C Journal of Carbon Research

*Article*

# Manganese Oxide Coated Carbon Materials as Hybrid Catalysts for the Application in Primary Aqueous Metal-Air Batteries

**Andreas Flegler [1,*], Sarah Hartmann [1,†], Henning Weinrich [2,†], Martina Kapuschinski [1,†], Jochen Settelein [1,†], Henning Lorrmann [1] and Gerhard Sextl [1,3]**

[1] Fraunhofer Institute for Silicate Research (ISC), Neunerplatz 2, 97082 Wuerzburg, Germany; sarah.hartmann@froetek.de (S.H.); martina.kapuschinski@isc.fraunhofer.de (M.K.); jochen.settelein@isc.fraunhofer.de (J.S.); henning.lorrmann@isc.fraunhofer.de (H.L.); gerhard.sextl@isc.fraunhofer.de (G.S.)

[2] Forschungszentrum Juelich, GmbH, Institute of Energy and Climate Research, IEK-9, 52425 Juelich, Germany; h.weinrich@fz-juelich.de

[3] Julius-Maximilians-University Wuerzburg, Roentgenring 11, 97070 Wuerzburg, Germany

* Correspondence: andreas.flegler@isc.fraunhofer.de; Tel.: +49-931-4100-565; Fax: +49-931-4100-570

† These authors contributed equally to this work.

Academic Editor: Rüdiger Schweiss
Received: 30 October 2015; Accepted: 2 February 2016; Published: 15 February 2016

**Abstract:** One of the major challenges of metal-air batteries is the impeded oxygen reduction reaction (ORR) during discharge occurring at the gas diffusion electrode (GDE) of the battery. Due to the impeded ORR, high overpotentials emerge and result in a loss of energy efficiency. In order to improve the latter, suitable catalysts have to be employed. Transition metal oxides like manganese oxides (e.g., $MnO_2$, $Mn_2O_3$, $Mn_3O_4$, $Mn_5O_8$, MnOOH) [1,2] are known as good and inexpensive materials for the ORR in alkaline media. A drawback of manganese oxide catalysts is the poor electrical conductivity. Hence, the approach presented in this work aims to enhance the catalytic activity of $Mn_3O_4$ and $\gamma$–$MnO_2$ by the incorporation of conductive carbon material into the pure manganese oxide. The resulting hybrid catalysts are prepared either by impregnation of Super C 65, Vulcan XC 72, and Kuraray YP 50F via a sol-gel technique employing a $MnO_2$ precursor sol or by direct precipitation of $Mn_3O_4$ or $\gamma$–$MnO_2$ particles in the presence of the carbon materials mentioned above. Investigations by rotating disc electrode (RDE) show a noticeably higher catalytic activity of the hybrid catalysts than for the pure materials. For verification of the results measured by RDE, screen printed GDEs are prepared and tested in Zn-air full cells.

**Keywords:** $\gamma$–$MnO_2$ catalyst; $Mn_3O_4$ catalyst; oxygen reduction reaction (ORR); gas diffusion electrode (GDE); aqueous metal-air battery; Zn-air battery; screen printing

## 1. Introduction

The global demand of energy storage systems for mobile and stationary applications is continuously growing. At present, lithium ion batteries (LIBs) are established in fields of mobile applications such as smart phones and notebooks. Due to higher theoretical specific energy in comparison to LIBs (387 Wh $kg^{-1}$ [3]) the metal-air technology (Li–$O_2$: 3503 Wh $kg^{-1}$ for non-aqueous electrolyte and 3582 Wh $kg^{-1}$ for aqueous electrolyte; Zn–$O_2$: 1086 Wh $kg^{-1}$ [3]; Na–$O_2$: 1605 Wh $kg^{-1}$ [4]) is a promising candidate for energy storage systems beyond LIBs [5–8].

In general, a metal-air battery consists of a metal anode and a gas diffusion electrode (GDE) as cathode separated by electrolyte and separator. The type of electrolyte depends on the anode material. In this article, we focus on GDEs for Zn-air batteries in which an aqueous alkaline electrolyte (such as

KOH (aq.)) can be employed [5,9]. Primary Zn-air batteries are commercially used as button cells for hearing heads with a theoretical specific capacity of 820 mAh $g^{-1}$ Zn and a theoretical cell voltage of 1.65 V [8].

In metal-air batteries, oxygen diffuses from ambient air through the GDE into the battery cell and is reduced at the catalytic centers of the GDE while the metal, in this case zinc, is oxidized. The ORR mechanism follows two different pathways in alkaline solution which are described in the following equations. Equation (1) describes the direct four electron mechanism ($n$ = 4). In this case $O_2$ is directly reduced to $OH^-$ ions.

$$O_2 + 2H_2O + 4e^- \rightarrow 4OH^- \text{ (0.401 V } vs. \text{ NHE)} \tag{1}$$

Equations 2 and 3 describe the indirect ORR mechanism with two reactions. Each step includes two electron transfers ($n$ = 2). In the first reaction (Equation (2)), $O_2$ is reduced forming a peroxide ion ($HO_2{}^-$). In the second reaction (Equation (3)) $HO_2{}^-$ is reduced to $OH^-$ [6,10].

$$O_2 + H_2O + 2e^- \rightarrow HO_2^- + OH^- \text{ (}-0.065 \text{ V } vs. \text{ NHE)} \tag{2}$$

$$HO_2^- + H_2O + 2e^- \rightarrow 3OH^- \text{ (0.867 V } vs. \text{ NHE)} \tag{3}$$

The ORR takes place at the *three-phase boundary* of the GDE where gaseous oxygen is adsorbed at the catalytically active centers and reduced to hydroxide ions, which are released into the aqueous electrolyte. The consumed electrons are transported through the solid carbon matrix [10].

The ORR exhibit high overpotentials which result in a change of the cell voltage during discharging from theoretical 1.65 V for Zn-air cells down to 1.2 V and below [9]. To reduce these overpotentials, suitable catalysts based on transition metal oxides like manganese oxides, perovskites, spinels or noble metals are required [5,7–9,11]. A detailed overview of investigated catalyst for Zn-air batteries was reported by Neburchilov *et al.* [12]. Especially manganese oxides exhibit a good catalytic activity for the ORR. Moreover, manganese oxides feature a good material availability, low costs and environmental compatibility. [13] Unfortunately, manganese oxides also feature a low electronic conductivity. The drawback can be overcome by the addition of conductive carbon which enhances the catalytic activity [13–17].

In this article, two approaches for a direct functionalization of different carbon materials with $Mn_3O_4/\gamma$–$MnO_2$ are discussed (Figure 1). In the first approach (Figure 1a) carbon is coated with a thin layer of $Mn_3O_4$ via sol-gel impregnation. Thereby, a hybrid catalyst is prepared which exhibits a thin catalytically active shell of $Mn_3O_4$ on an electrically conductive carbon core such as Super C 65 or Vulcan XC 72. In the second approach (Figure 1b) different forms of manganese oxides are precipitated in the direct presence of carbon. Depending on the carbon material, $\gamma$–$MnO_2$ or $Mn_3O_4$ particles grow on the carbon materials with strong adhesion. Both $\gamma$–$MnO_2$ and $Mn_3O_4$ have been further investigated as catalysts for ORR in GDEs [1,2]. In this paper, all hybrid catalysts are referred to as $Mn_xO_y$@C.

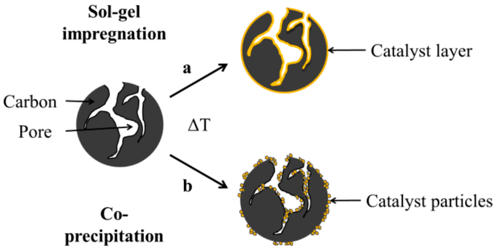

**Figure 1.** Different synthesis strategies for $Mn_xO_y$@C; (**a**) sol-gel impregnation of carbon and (**b**) co-precipitation of $\gamma$–$MnO_2$ or $Mn_3O_4$ in presence of carbon.

Finally, the synthesized hybrid catalysts are introduced into the reactive layer of a GDE. In Figure 2, the preparation process of the GDEs is depicted. A nickel mesh, the current collector, is hot pressed on the microporous carbon layer of a commercial gas diffusion layer (GDL). Afterwards, the reactive layer consisting of catalyst, carbon, and binder is screen printed on the GDL/nickel mesh substrate.

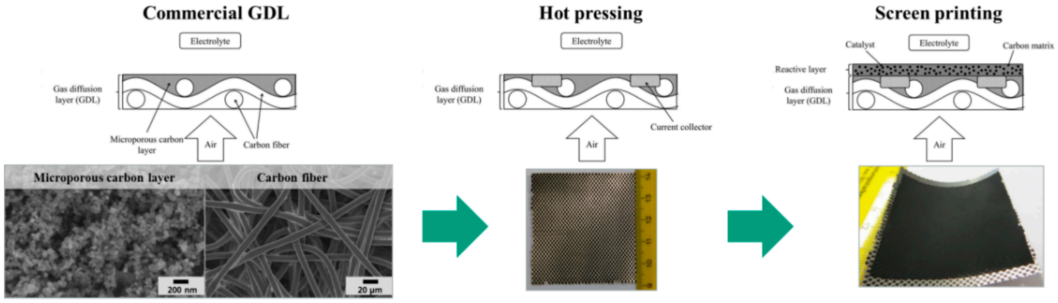

**Figure 2.** Schematic preparation of a gas diffusion electrode (GDE).

## 2. Results and Discussion

### 2.1. Characterization of Pure and Hybrid Catalysts

The structural properties of all investigated catalysts are analyzed by scanning electron microscopy (SEM), X-ray diffraction (XR), thermogravimetric differential thermal analysis (TG/DTA) and Brunauer-Emmett-Teller (BET) method to evaluate the differences between pure $\gamma$–$MnO_2$, $Mn_3O_4$, carbon materials and hybrid catalysts.

$\gamma$-$MnO_2$ is synthesized via co-precipitation of $MnSO_4 \cdot H_2O$ and $(NH_4)_2S_2O_8$ according to a procedure presented by Xi *et al.* [18] and Li *et al.* [19]. Figure 3a depicts a representative SEM image of spherical catalyst particles of about 4 μm diameter formed by needle-shaped nanochrystals. The associated XRD pattern (Figure 3b) indicates the crystal structure of $\gamma$–$MnO_2$ which is a crystallographic deformation of $\alpha$–$MnO_2$ (ramsdellite) and $\beta$–$MnO_2$ (pyrolusite). According to Gyenge and Drillet [20] the peaks at $2\theta$: 37.5° (101), 43.0° (111), 57.0° (211), and 67.5° (310) can be identified as pyrolusite (JCPDS: 98-002-0229) and the small peak at $2\theta = 22.0$ (011) matches with ramsdellite (JCPDS: 98-002-0228). The broad peaks are attributed to nanoscale $\gamma$–$MnO_2$ crystallites. The second investigated pure catalyst is a commercial $Mn_3O_4$ (Sigma Aldrich, purity: 97%). The SEM image in Figure 3c depicts agglomerated $Mn_3O_4$ particles with a diameter of approximately 1 μm for the primary particles. The corresponding XRD pattern (Figure 3d) displays the expected $Mn_3O_4$ spinel crystal structure with the following characteristic reflections at 18.0° (101), 28.5° (110), 37.2° (101), 40.9° (200), 42.6° (111), 56.5° (211), 59.2° (220), 64.7° (002), 67.1° (310), 72.1° (301), 72.3° (112) (JCPDS: 024-0734). In addition to the crystal structure, $\gamma$-$MnO_2$ and $Mn_3O_4$ differ in their specific surface areas. Due to its urchin like structure, $\gamma$–$MnO_2$ exhibits a much higher specific surface area ($S_{BET} = 104\ m^2\ g^{-1}$) than the smooth $Mn_3O_4$ particles ($S_{BET} = 1\ m^2\ g^{-1}$).

To investigate the influence of carbon materials on the hybrid catalysts, three carbon materials with different properties such as specific surface area or carbon modification were selected (Table 1). Super C 65 is a carbon black material which is used as a conductive agent in LIB electrodes [21] and Vulcan XC 72 is as catalyst support in fuel cells [22] which is employed due to its high electric conductivity. The intention in the application of Super C 65 and Vulcan XC 72 is to support the electric conductivity of the hybrid catalyst through a direct link between manganese oxide and carbon black. For a further study on the influence of an increased surface area, Kuraray YP 50F, is chosen. Kuraray YP 50F is an activated carbon material with a surface area of $S_{BET} = 1485\ m^2\ g^{-1}$ which is known for its application in electric double layer capacitors (ELDC) [23].

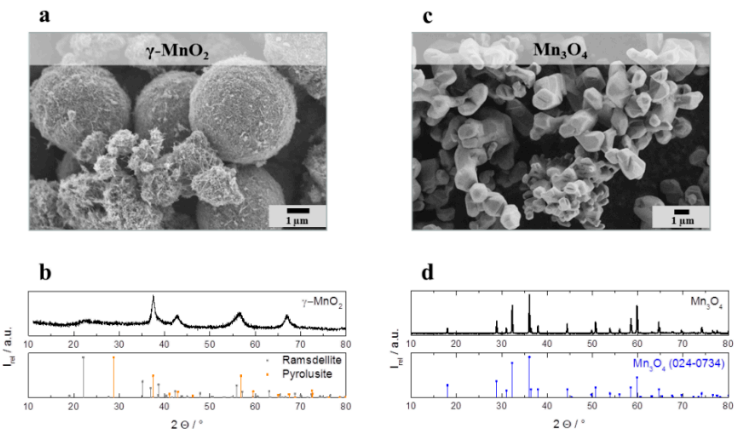

**Figure 3.** (**a**) Scanning electron microscope (SEM) image and (**b**) X-ray diffraction pattern of as prepared γ-$MnO_2$ particles. (**c**) SEM image and (**d**) X-ray diffraction pattern of commercial $Mn_3O_4$ particles.

**Table 1.** Used carbon materials for hybrid catalysts.

| Carbon Material | Manufacturer | Specific Surface Area $S_{BET}$ ($m^2\ g^{-1}$) | Carbon Modification |
|---|---|---|---|
| Super C 65 | Imerys (CHE) | 63 | carbon black |
| Vulcan XC 72 | Cabot (USA) | 230 | carbon black |
| Kuraray YP 50F | Kuraray Chemical Co., LTD (JPN) | 1485 | activated carbon |

The middle row of the SEM images in Figure 4a depicts the pure carbon materials before modification. The fine particulate morphology of both carbon black materials (Super C 65 and Vulcan XC 72) is clearly distinguishable from the coarse irregular shape of the activated carbon particles (Kuraray YP 50F).The first row of the SEM images in Figure 4b pictures the carbon materials coated by sol-gel impregnation. In the SEM images, not much difference in the surface morphology between the pure carbon materials and the coated carbon materials is found. The X-ray diffraction patterns of the sol-gel hybrid catalysts (Figure 5a) show the spinel structure of $Mn_3O_4$ after crystallization for 4 h at 300 °C.

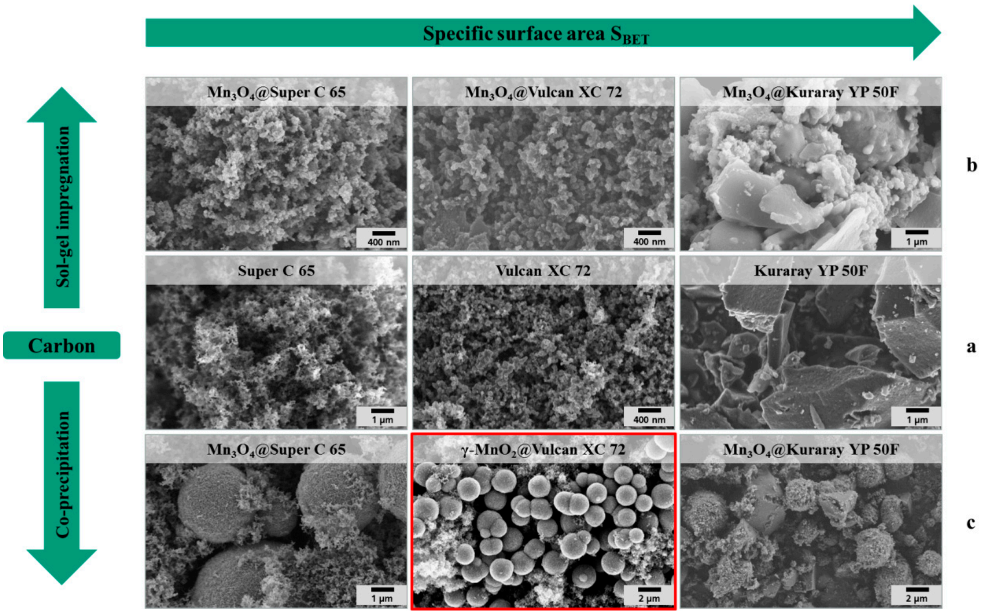

**Figure 4.** SEM images of (**a**) pure carbon materials, (**b**) hybrid catalysts synthesized via sol-gel impregnation and (**c**) hybrid catalysts synthesized via co-precipitation.

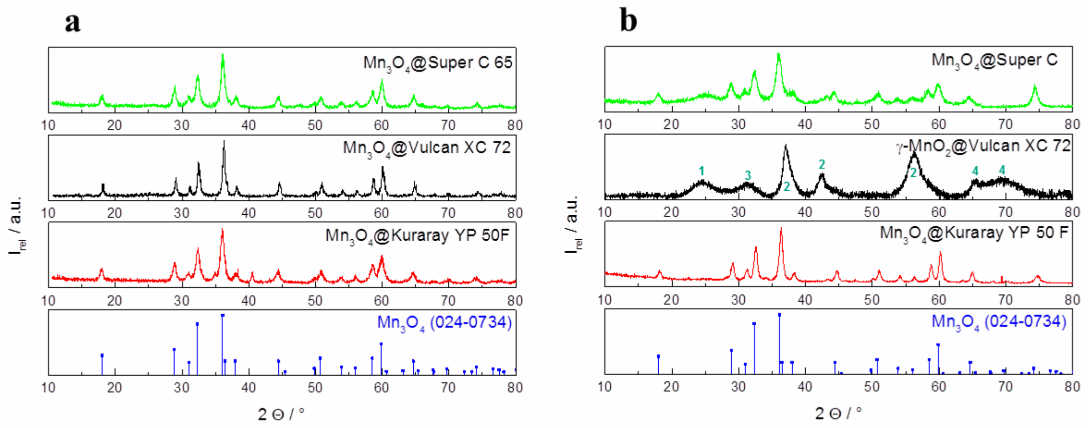

**Figure 5.** X-ray diffraction pattern of hybrid catalysts synthesized via (**a**) sol-gel impregnation and (**b**) co-precipitation.

Figure 4c shows the SEM images of the hybrid catalysts which are synthesized via co-precipitation. As a result of this synthesis method, spherical manganese oxide particles with a diameter of a few microns are formed and embedded into the carbon matrix. The X-ray diffraction patterns of the hybrid manganese oxide catalyst in the presence of Super C 65 and Kuraray YP 50F (Figure 5b) offer the crystal structure of $Mn_3O_4$. In the presence of Vulcan XC 72 a different X-ray diffraction pattern results with the product $\gamma$–$MnO_2$@Vulcan XC 72. The first peak (marked as 1) at $2\theta = 24.5°$ can be correlated with pure Vulcan XC 72. According to the X-ray diffraction of $\gamma$–$MnO_2$ (Figure 3b) the peaks (marked as 2) at $2\theta$: 37.5° (101), 43.0° (111), and 57.0° (211) can be identified as pyrolusite (JCPDS: 98-002-0229). The peak marked as 3 at $2\theta = 31.8°$ (014) matches with $MnCO_3$ (JCPDS: 98-003-7242) and the peaks marked as 4 at $2\theta$: 65.0° (200) and 69.9° (190) matches with $\gamma$–$MnO_2$ (JCPDS: 98-015-0462).

In Figure 6a, TG/DTA measurements of pure $\gamma$–$MnO_2$ and $\gamma$–$MnO_2$@Vulcan XC 72 synthesized via co-precipitation are plotted. Therein, the first exothermic peak for $\gamma$–$MnO_2$ at 206 °C and at 240 °C for $\gamma$–$MnO_2$@Vulcan XC 72 is related to the formation of $\gamma$–$MnO_2$. Furthermore, the endothermic peaks for $\gamma$–$MnO_2$ at 547 °C and at about 950 °C result from the reduction of $MnO_2$ to $Mn_2O_3$ to $Mn_3O_4$ [24]. The big mass loss of about 35 wt % between 400 and 600 °C in the TG curve of $\gamma$–$MnO_2$@Vulcan XC 72 is mainly related to the decomposition of Vulcan XC 72.

The TG/DTA curves of $Mn_3O_4$@Kuraray YP 50F (Precipitation) in Figure 6b represent a different curve progression. At the first mass loss of about 18 wt % between RT and 100 °C mainly $H_2O$ is detected. The second big mass loss (50 wt %) between 200 and 500 °C as well as the exothermic DTA peak at 368 °C is related to the decomposition of Kuraray YP 50F. The reason for this different TG/DTA behavior between the precipitated hybrid catalysts (based on Vulcan XC 72 and Kuraray YP 50F) can be seen in the pH value of the carbon materials. Kuraray YP 50F and Super C 65 exhibit an alkaline pH value of 9. However, Vulcan XC 72 shows a neutral pH value of about 7. The co-precipitation reaction of $\gamma$–$MnO_2$ without carbon material is proton catalyzed, which means that by addition of Vulcan XC 72 with a neutral pH value the same reaction takes place and the product $\gamma$–$MnO_2$ is formed. The addition of an alkaline material such as Kuraray YP 50F or Super C 65 results in the formation of $Mn_3O_4$ as reaction product. Dhaouadi *et al.* [25] reported the formation of $Mn_3O_4$ in alkaline media. In this reaction, first $Mn(OH)_2$ is formed, which decomposes into MnO and $H_2O$ (mass loss in Figure 6b between RT and 100 °C in the TG curve). During heat treatment MnO is oxidized to $Mn_3O_4$.

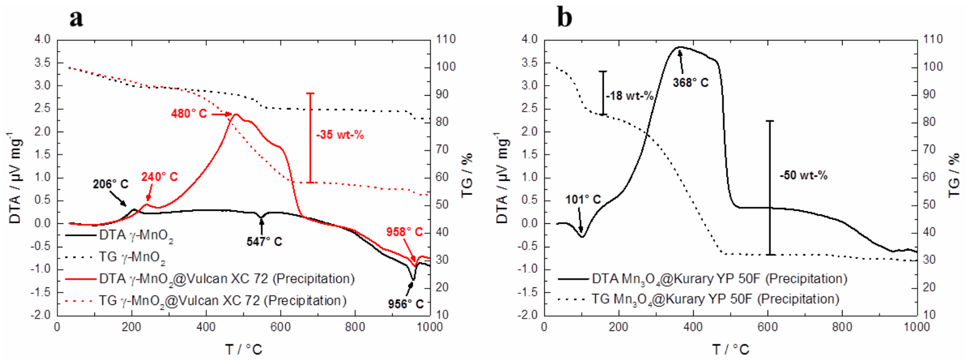

**Figure 6.** Thermogravimetric differential thermal analysis (TG/DTA) measurements (before tempering at 300 °C) of (**a**) pure $\gamma$–$MnO_2$ and $\gamma$–$MnO_2$@Vulcan XC 72 synthesized via co-precipitation; (**b**) $Mn_3O_4$@Kuraray YP 50F synthesized via co-precipitation.

In Table 2, the specific surface areas of all hybrid catalyst materials are depicted. By comparing these values it can be seen that, the co-precipitated hybrid catalysts show a higher specific surface area than the sol-gel impregnated ones, e.g., for Kuraray YP 50F $S_{BET}$ (Sol) = 239 m² g$^{-1}$ *vs.* $S_{BET}$ (Precipitation) = 869 m² g$^{-1}$. However, the co-precipitated hybrid catalysts have a higher carbon content (extracted from TG/DTA data). Especially in the case of Vulcan XC 72 ($S_{BET}$ = 230 m² g$^{-1}$) and Kuraray YP 50F ($S_{BET}$ = 1485 m² g$^{-1}$) the pure carbon materials have a much higher specific surface area than pure $\gamma$–$MnO_2$ ($S_{BET}$ = 104 m² g$^{-1}$) or $Mn_3O_4$ ($S_{BET}$ = 1 m² g$^{-1}$). Additionally, the SEM images of Figure 4 demonstrate that in the case of so-gel impregnated hybrid catalysts the carbon materials are covered with a $Mn_3O_4$ shell. This might causes a blocking of the carbon pores and reduces the specific surface area of these hybrid catalysts in comparison to the corresponding carbon material. For the co-precipitated catalysts $\gamma$–$MnO_2$ or $Mn_3O_4$ particles are present adjacent to the carbon materials. Therefore, the specific surface area results in an arithmetic mean of carbon and manganese oxide which is much higher compared to the sol-gel impregnated hybrid catalyst.

**Table 2.** Structural properties of all investigated materials.

| Catalyst | Synthesis Pathway | Carbon Content of Hybrid Catalyst (wt %) | Specific Surface Area $S_{BET}$ (m² g$^{-1}$) |
|---|---|---|---|
| $\gamma$-$MnO_2$ | Co-precipitation | 0 | 104 |
| $Mn_3O_4$ | Sigma Aldrich | 0 | 1 |
| $Mn_3O_4$@Super C 65 | Sol-gel impregnation | 32 | 52 |
| $Mn_3O_4$@Super C 65 | Co-precipitation | 35 | 73 |
| Super C 65 | | 100 | 63 |
| $Mn_3O_4$@Vulcan XC 72 | Sol-gel impregnation | 24 | 50 |
| $\gamma$-$MnO_2$@Vulcan XC 72 | Co-precipitation | 39 | 116 |
| Vulcan XC 72 | | 100 | 230 |
| $Mn_3O_4$@Kuraray YP 50F | Sol-gel impregnation | 18 | 239 |
| $Mn_3O_4$@Kuraray YP 50F | Co-precipitation | 28 | 869 |
| Kuraray YP 50F | | 100 | 1485 |

### 2.2. *Electrocatalytic Activity of Pure and Hybrid Catalysts*

The electrocatalytic activity for the oxygen reduction reaction (ORR) is measured by rotating disc electrode (RDE). The polarization curves of all investigated catalysts are depicted in Figure 7a–c. All measurements are carried out in $O_2$-saturated 1 M KOH (aq.) solution at a rotation rate of 900 rpm. For comparison of the different catalysts the onset potential at −1 mA cm$^{-2}$ and the corresponding limiting current density at −0.5 V *vs.* Hg/HgO are employed (Table 3). The higher the onset potential of the reaction is, the lower the overpotentials for the ORR.

In Figure 7a the polarization curves of $Mn_3O_4$@Super C 65 (Sol) and $Mn_3O_4$@Super C 65 (Precipitation) are compared to pure catalysts $Mn_3O_4$ and $\gamma$–$MnO_2$ as well as to pure Super C

65. The catalytic activity of the latter materials can be ranked in the following ascending order: $Mn_3O_4$ < Super C 65 < $\gamma$–$MnO_2$. Furthermore, it can be seen that the sol-gel impregnation of Super C 65 with $Mn_3O_4$ reduces the onset potential compared to Super C 65 by 111 mV *vs.* Hg/HgO. At the same time, the limiting current density of $Mn_3O_4$@Super C 65 (Sol) is increased by 0.8 mA cm$^{-2}$ compared to $Mn_3O_4$. The highest ORR activity in this plot is detected for $Mn_3O_4$@Super C 65 synthesized via co-precipitation. This hybrid catalyst exhibits an onset potential for ORR of −203 mV vs Hg/HgO and a limiting current density of −2.38 mA cm$^{-2}$. These results show that the combination of carbon and catalyst strongly enhances the catalytic activity for the ORR in comparison to pure materials Super C 65 and $Mn_3O_4$ [13,15,16].

The same ranking of ORR activity is also found for the hybrid catalysts containing Vulcan XC 72 and Kuraray YP 50F as carbon material (Figure 7b–c). Independent of the used carbon material, again the catalysts synthesized via co-precipitation show higher ORR activity than the sol-gel impregnated ones (e.g., the difference in onset potentials of the hybrid catalysts based on Super C 65: 19 mV; Vulcan XC 72: 86 mV; Kuraray YP 50F: 35 mV and the difference in limiting current density for Super C 65: 0.70 mA cm$^{-2}$, Vulcan XC 72: 0.77 mA cm$^{-2}$ and Kuraray YP 50F: 0.62 mA cm$^{-2}$). One reason for this could be that the pores of the carbon as well as of the manganese oxide are more accessible for oxygen, which results in a large three-phase boundary layer for the reduction of oxygen to $OH^-$. Another reason for the higher catalytic activity of the co-precipitated catalysts compared to the sol-gel impregnated ones could be the presence of a small amount of Ag in the co-precipitated hybrid catalysts. $AgNO_3$ is used as catalyst for the co-precipitation synthesis and after heat treatment a little amount of Ag is contained in the co-precipitated catalysts and perhaps gives an additional catalytic effect for the ORR.

For pure carbon materials, Kuraray YP 50F shows the highest onset potential of −194 mV *vs.* Hg/HgO and almost the same limiting current density of −1.38 mA cm$^{-2}$ as Vulcan XC 72. Super C 65 exhibits the lowest limiting current density of −1.09 mA cm$^{-2}$ and the poorest onset potential among the investigated carbon materials of −333 mV *vs.* Hg/HgO. This behavior can be correlated to the specific surface area of the carbon materials—the higher the specific surface area the more active the carbon material for the ORR. In contrast to this, hybrid catalysts show a different behavior. In this case, it appears that the surface area has not such a big influence on the ORR activity.

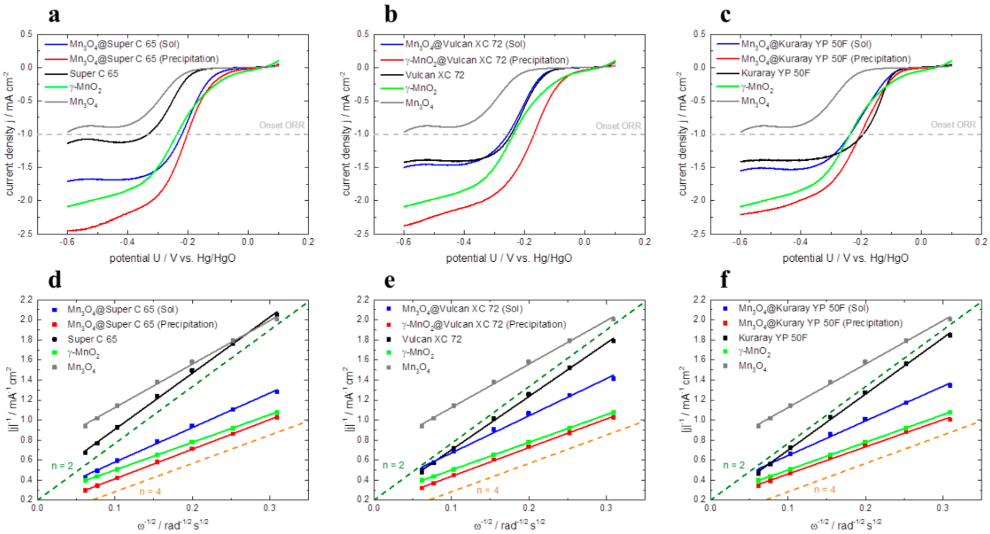

**Figure 7.** **O**xygen reduction reaction (ORR) polarization curves of pure $\gamma$–$MnO_2$, $Mn_3O_4$, pure carbon materials and hybrid catalysts based on (**a**) Super C 65, (**b**) Vulcan XC 72, (**c**) Kuraray YP 50F in $O_2$-saturated 1 M KOH (aq.) solution at a rotations rate of 900 rpm and a scan rate of 5 mV s$^{-1}$. Corresponding Koutecky-Levich plots of pure $\gamma$–$MnO_2$, $Mn_3O_4$, pure carbon materials and hybrid catalysts based on (**d**) Super C 65, (**e**) Vulcan XC 72, (**f**) Kuraray YP 50F at −0.5 V *vs.* Hg/HgO.

The number of electrons $n$ transferred during ORR and thus the underlying mechanism of the ORR (according to Equations (1–3)) is evaluated by the Koutecky-Levich equation [10,26,27]:

$$\frac{1}{j} = \frac{1}{j_k} + \frac{1}{B\omega^{1/2}} \tag{4}$$

$$B = 0.62\, n\, F\, A\, \nu^{-1/6}\, c_{O_2}\, D_{O_2}^{2/3} \tag{5}$$

($j$: measured current density (at $-0.5$ V *vs.* Hg/HgO); $j_k$: kinetic current density; $\omega$: angular velocity; $B$: slope of the regression line; $n$: number of electrons transferred; $F$: faraday constant; $\nu$: kinetic viscosity of the electrolyte, $c_{O_2}$: $O_2$ concentration in the electrolyte; $D_{O_2}$: diffusion coefficient of $O_2$ in the electrolyte).

The corresponding Koutecky-Levich plots at –0.5 V *vs.* Hg/HgO of all investigated catalysts are presented in Figure 7. From the slope of the regression line, the number of transferred electrons $n$ can be calculated according to Equation 5 (Table 3). All investigated pure carbon materials catalyze the ORR via the indirect two electron mechanism ($n$ = 2) [10,17,28,29]. Pure γ–$MnO_2$ and the hybrid catalysts which are synthesized via co-precipitation follow the direct four electron mechanism ($n$ = 4) [7,17]. The hybrid catalysts synthesized via sol-gel impregnation exhibit electron transfer numbers in the area of about $n$ = 3. In this case both the direct four electron mechanism as well as the indirect two electron mechanism takes place.

**Table 3.** Electrochemical properties of all investigated catalyst materials.

| **Catalyst** | **Synthesis Pathway** | **Onset Potential at −1 mA cm$^{-2}$ (mV *vs.* Hg/HgO)** | **Limiting Current Density at −0.5 V *vs.* Hg/HgO (mA cm$^{-2}$)** | **Electron Transfer Number *n*** |
|---|---|---|---|---|
| γ-$MnO_2$ | Co-precipitation | −238 | −1.97 | 4 |
| $Mn_3O_4$ | Sigma Aldrich | - | −0.88 | 2.6 |
| $Mn_3O_4$@Super C 65 | Sol-gel impregnation | −222 | −1.68 | 3.3 |
| $Mn_3O_4$@Super C 65 | Co-precipitation | −203 | −2.38 | 4 |
| Super C 65 | | −333 | −1.09 | 2 |
| $Mn_3O_4$@Vulcan XC 72 | Sol-gel impregnation | −256 | −1.46 | 3.0 |
| γ-$MnO_2$@Vulcan XC 72 | Co-precipitation | −170 | −2.23 | 4 |
| Vulcan XC 72 | | −245 | −1.39 | 2 |
| $Mn_3O_4$@Kuraray YP 50F | Sol-gel impregnation | −238 | −1.51 | 3.3 |
| $Mn_3O_4$@Kuraray YP 50F | Co-precipitation | −203 | −2.13 | 4 |
| Kuraray YP 50F | | −194 | −1.38 | 2 |

### 2.3. Discharge Behavior in Zn-Air Full Cells

Subsequent to the RDE characterization, all investigated catalysts and pure carbon materials were introduced into the reactive layer of a GDE (Figure 3). For comparison, also pure carbon materials were processed as well. In Figure 8, the surface morphology of the reactive layer containing 20 wt % γ–$MnO_2$@Vulcan XC 72 (Precipitation) hybrid catalysts is exemplarily represented. The homogeneous distribution of the hybrid catalyst (red) is visualized by EDS mapping.

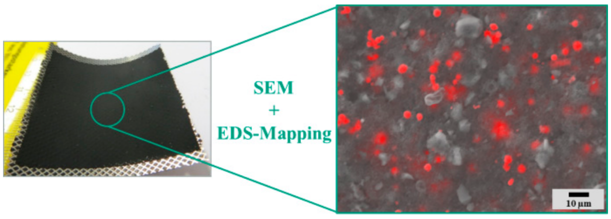

**Figure 8.** SEM image of the reactive layer of an as prepared GDE containing γ-$MnO_2$@Vulcan XC 72 (precipitation) including energy dispersive X-ray spectroscopy (EDS) mapping (red color corresponds to manganese).

The prepared GDEs are tested in Zn-air full cells employing 6 M KOH (aq.) as electrolyte, zinc granules as anode material, and a constant flow of ambient air in a commercial El-Cell® ECC-Air test cell. In Figure 9, the resulting polarization curves of the GDEs are plotted. In graphs a, b, and c the polarization curves of the hybrid catalysts are compared to pure $\gamma$–$MnO_2$ and $Mn_3O_4$ catalysts as well as the corresponding carbon material to investigate the impact of manganese oxide coating on full cell performance. Within the graphs it can be seen that all cells containing hybrid catalysts via co-precipitation (red lines) show a higher cell voltage than cells prepared with sol-gel impregnated catalysts (blue lines). Thus, it appears that the polarization behavior of co-precipitated catalysts is much better than the polarization behavior of sol-gel impregnated catalysts. This behavior can be correlated with the RDE polarization curves.

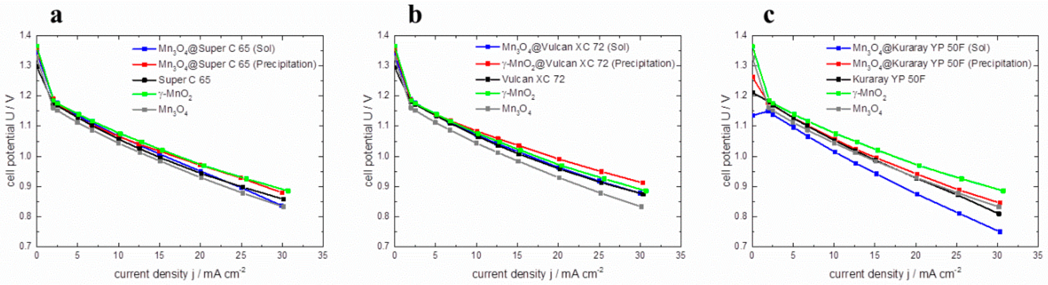

**Figure 9.** Polarization curves of pure $\gamma$–$MnO_2$, $Mn_3O_4$, pure carbon materials and hybrid catalysts based on (**a**) Super C 65, (**b**) Vulcan XC 72, (**c**) Kuraray YP 50 F, in Zn-air full cells.

The discharge curves of all prepared GDEs are presented in Figure 10. Just like in the polarization behavior measured by RDE and in full cells, the GDEs containing the co-precipitated hybrid catalysts exhibit higher specific capacities compared to the sol-gel impregnated ones (for Super C 65: 75 mAh $g^{-1}$ higher, for Vulcan XC 72: 132 mAh $g^{-1}$ higher and for Kuraray YP 50F: 146 mAh $g^{-1}$ higher) as well as the pure materials. The support of carbon with the co-precipitated synthesis route improves the discharge and polarization behavior. Additionally the amount of manganese oxide is strongly reduced in the hybrid catalysts. The highest specific capacity of the hybrid catalyst is reached with Vulcan XC 72 with 449 mAh $g^{-1}$ (discharge time: 10.75 h) and a discharge plateau of 1.11 V at 200 mAh $g^{-1}$. In this case the specific capacity can be increased by 25% (with 39% less amount of $\gamma$–$MnO_2$) compared to pure $\gamma$–$MnO_2$. This improved behavior correlates to the RDE polarization curves of $\gamma$–$MnO_2$@Vulcan XC 72 (precipitation). In the publication of Li *et al.* [13] a Zn-air discharge curve of a GDE with a Vulcan XC 72 / $\alpha$-$MnO_2$ (1:1) mixed catalyst is displayed which is discharged for 11.5 h (at 10 mA/cm²) and exhibits a discharge plateau of 1.2 V. These results are comparable with the here presented hybrid catalyst $\gamma$–$MnO_2$@Vulcan XC 72 synthesized by co-precipitation. The electrochemical properties of all investigated GDEs are shown in Table 4.

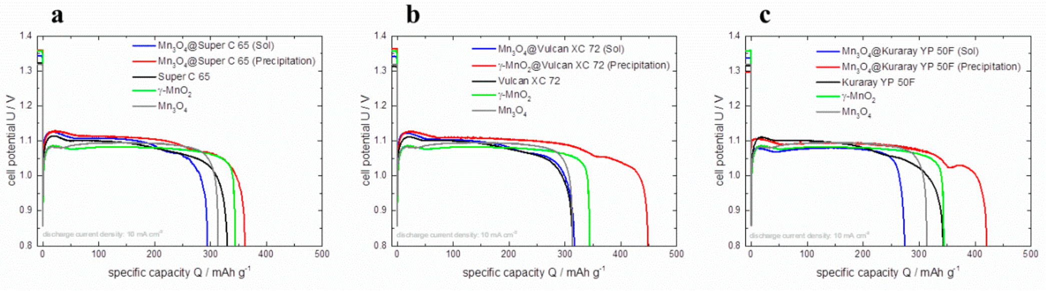

**Figure 10.** Discharge curves of pure $\gamma$–$MnO_2$, $Mn_3O_4$, pure carbon materials and hybrid catalysts based on (**a**) Super C 65, (**b**) Vulcan XC 72, (**c**) Kuraray YP 50F in Zn-air full cells at a constant current density of 10 mA $cm^{-2}$.

**Table 4.** Electrochemical properties of all investigated gas diffusion electrodes (GDEs).

| Catalyst | Synthesis Pathway | Cell Potential at 30 mA cm$^{-2}$ (V) | Cell Potential at 200 mAh g$^{-1}$ (V) | Specific Capacity (mAh g$^{-1}$) |
|---|---|---|---|---|
| $\gamma$-$MnO_2$ | Co-precipitation | 0.89 | 1.08 | 344 |
| $Mn_3O_4$ | Sigma Aldrich | 0.84 | 1.10 | 314 |
| $Mn_3O_4$@Super C 65 | Sol-gel impregnation | 0.84 | 1.09 | 295 |
| $Mn_3O_4$@Super C 65 | Co-precipitation | 0.88 | 1.10 | 362 |
| Super C 65 | | 0.86 | 1.08 | 330 |
| $Mn_3O_4$@Vulcan XC 72 | Sol-gel impregnation | 0.86 | 1.08 | 317 |
| $\gamma$-$MnO_2$@Vulcan XC 72 | Co-precipitation | 0.91 | 1.11 | 449 |
| Vulcan XC 72 | | 0.87 | 1.08 | 314 |
| $Mn_3O_4$@Kuraray YP 50F | Sol-gel impregnation | 0.75 | 1.08 | 275 |
| $Mn_3O_4$@Kuraray YP 50F | Co-precipitation | 0.85 | 1.10 | 421 |
| Kuraray YP 50F | | 0.81 | 1.08 | 343 |

## 3. Experimental Section

### 3.1. Synthesis of Catalysts

#### 3.1.1. Co-Precipitation

The synthesis via co-precipitation was based on [18,19,30]. $AgNO_3$ (Alfa Aesar) solution as catalyst was added to an equimolar aqueous solution of $MnSO_4 \cdot H_2O$ (Sigma Aldrich) and $(NH_4)_2S_2O_8$ (Sigma Aldrich). After approximately 60 h and by the oxidative effect of $AgNO_3$, manganese oxide particles of low solubility were formed. To receive the intended manganese oxide structure, the particles were tempered for 4 h at 300 °C in ambient air.

The same synthesis was used to prepare hybrid catalysts. In this case, carbon materials were added to the aqueous solution of $MnSO_4$ $H_2O$, $(NH_4)_2S_2O_8$ and $AgNO_3$.

#### 3.1.2. Sol-Gel Impregnation

In order to prepare a stable manganese oxide sol, $Mn(NO_3)_2$ (Sigma Aldrich) was dissolved in 3 wt % acetylacetone (Fluka Chemie) and 97 wt % propylene glycol monomethyl ether (Merck). After two days, the sol was diluted and stabilized with Superonic F108 (Fluka Chemie) resulting in a manganese oxide content of 1.5 wt %. In the subsequent step, different carbon materials were added to the sol and autoclaved for 5 h at 200 °C. To receive the intended manganese oxide structure on carbon, the hybrid catalysts were tempered for 4 h at 300 °C in ambient air.

### 3.2. Materials Characterization

All catalysts were analyzed by powder X-ray diffraction (XRD, Cu-$K_\alpha$ radiation, Philips PW 1730/10) at an angular speed of 0.02 s$^{-1}$ in the range from $2\theta = 10$ to $2\theta = 80$.

The morphology of these catalysts and as well as the structure of GDEs were investigated by Scanning Electron Microscopy (SEM, Zeiss Supra 25). The presence of manganese oxide in the GDEs was detected by Energy Dispersive X-ray Spectroscopy (EDS, EDAX). The specific surface area of all catalysts was calculated by the Brunauer-Emmett-Teller (BET) method from the data of $N_2$ adsorption/desorption isotherms (Quantachrom Autosorb-3B). The carbon content of each hybrid catalyst was evaluated by thermogravimetric analysis and differential thermal analysis (TG/DTA, Netzsch STA 449 C) in synthetic air with a heating rate of 10 K min$^{-1}$ from room temperature to 1000 °C.

### 3.3. Preparation of Gas Diffusion Electrodes (GDE)

The gas diffusion electrodes GDE consisted of a commercially gas diffusion layer GDL (Freudenberg FCCT SE & Co. KG, H2315 C2), a nickel mesh as current collector and a reactive layer in which the catalysts were embedded (Figure 2). The GDL was built up of a microporous carbon layer at the electrolyte facing side and of carbon fibers at the air facing side. In a first step, the nickel mesh was hot pressed onto the microporous layer of the GDL. In a second step, a slurry, composed of 20 wt % catalyst, 45 wt % conductive carbon black (Super C 65, Imerys), 20 wt % activated carbon (Kuraray YP 50F , Kuraray), 15 wt % PTFE (Sigma Aldrich, $\leqslant$12 μm) and terpineol as solvent (Fluka Chemie, 65% α-terpineol, 10% β-terpineol, 20% γ-terpineol) was mixed in a speedmixer (Hauschild DAC 150 FVZ) and coated on this substrate via screen printing (Ekra X1-SL). After drying at 100 °C for 1 h, a homogeneous reactive layer with a thickness of about 30 μm was obtained.

### *3.4. Electrochemical Measurements*

#### 3.4.1. Rotating Disc Electrode (RDE)

The electrochemical activity of all catalysts was investigated by rotating disc electrode (RDE, Pine Instruments, potentiostat: Autolab M101). Linear sweep voltammetry (LSV) was performed in $O_2$-saturated 1 M KOH(aq.). For the preparation of the working electrode, 20 mg catalyst was dispersed in 7.96 mL deionized water, 2.0 mL *n*-propanol (Sigma Aldrich) and 0.04 mL of a Nafion solution (5 wt %, Sigma Aldrich) under ultrasonic mixing (Sonics & Materials VCX130) for 15 min. Then 10 μL of this homogeneous suspension were dropped onto the polished surface of a glassy carbon electrode (5 mm diameter, Pine Instruments) and dried at 35 °C for 15 min. To complete the three electrode assembly, a glassy carbon rod and a Hg/HgO/1 M KOH (aq.) were used as counter electrode and reference electrode. As electrolyte $O_2$-saturated 1 M KOH(aq.) was used, the LSV was carried out under a constant flow of pure $O_2$ at various rotations rates of 100, 150, 240, 400, 900, 1600, 2500 rpm with a scan rate of 5 mV $s^{-1}$ and in a potential range between 0.1 V and −0.6 V *vs.* Hg/HgO. All experiments were performed three times. The ORR onset potential was determined at −1 mA $cm^{-2}$ [31]. The limiting current density was taken at −0.5 V *vs.* Hg/HgO at a rotation rate of 900 rpm. The number of electrons *n*, transferred during ORR, was calculated by the Koutecky-Levich equation (Equation 5).

#### 3.4.2. Full Cell Assembly

The Zn-air full cell experiments were performed in El-Cell® ECC-Air test cells (EL-Cell®). Herein, the prepared GDEs with a diameter of 18 mm were used as cathode, 0.609 g zinc granules (Grillo GHN20-10) as anode, 6 M KOH (aq.) as electrolyte and a glass fiber separator (EL-Cell®, ECC-01-0012-C/L). During all measurements, the GDE was provided with a constant flow of ambient air at room temperature.

The discharge curves were recorded at a battery tester (Maccor Series 4000) with a constant current density of 10 mA $cm^{-2}$. The polarization curves were taken at different constant current densities between 0 and 30 mA $cm^{-2}$.

## 4. Conclusions

In this work, two different synthesis pathways were shown to combine carbon materials with manganese oxide catalysts. The aim was to increase the catalytic activity of manganese oxides by the support of carbon with a high electric conductivity. The sol-gel impregnation of carbon with manganese oxide results in a core-shell catalyst—whereas the co-precipitation of manganese oxide in presence of carbon results in a hybrid catalyst with spherical manganese oxide particles on carbon. The co-precipitated hybrid catalysts, especially $\gamma$–$MnO_2$@Vulcan XC 72, show the highest catalytic activity for the ORR among the analyzed catalysts measured by RDE. $\gamma$–$MnO_2$@Vulcan XC 72 also exhibits the best discharge and polarization behavior in GDEs measured in Zn-air full cells. In summary, the combination of carbon material with manganese oxide ($Mn_3O_4$ or $\gamma$–$MnO_2$), especially via the co-precipitation method, provides an electrochemically more active hybrid catalyst than the pure materials.

**Acknowledgments:** This work was financially supported by the BFS (Bayerische Forschungsstiftung) as part of the ZiBa (Zink-Luft Batterien als stationäre Energiespeicher) project. The authors would like to thank all project partners at VARTA microbattery GmbH, University of Bayreuth (Lehrstuhl für Werkstoffverarbeitung) and Eckart GmbH.

**Author Contributions:** Andreas Flegler and Sarah Hartmann conceived and designed the experiments; Andreas Flegler, Martina Kapuschinski and Jochen Settelein performed the experiments; Andreas Flegler, Sarah Hartmann and Henning Weinrich analyzed the data; Andreas Flegler wrote the paper; Henning Lorrmann and Gerhard Sextl supervised the whole work.

**Conflicts of Interest:** The authors declare no conflict of interest.

## References

1. Mao, L. Mechanistic study of the reduction of oxygen in air electrode with manganese oxides as electrocatalysts. *Electrochim. Acta* **2003**, *48*, 1015–1021. [CrossRef]
2. Mao, L.; Sotomura, T.; Nakatsu, K.; Koshiba, N.; Zhang, D.; Ohsaka, T. Electrochemical characterization of catalytic activities of manganese oxides to oxygen reduction in alkaline aqueous solution. *J. Electrochem. Soc.* **2002**, *149*, A504–A507. [CrossRef]
3. Bruce, P.G.; Freunberger, S.A.; Hardwick, L.J.; Tarascon, J.-M. Li-$O_2$ and Li-S batteries with high energy storage. *Nat. Mater.* **2012**, *11*, 19–29. [CrossRef] [PubMed]
4. Hartmann, P.; Bender, C.L.; Vračar, M.; Dürr, A.K.; Garsuch, A.; Janek, J.; Adelhelm, P. A rechargeable room-temperature sodium superoxide ($NaO_2$) battery. *Nat. Mater.* **2012**, *12*, 228–232. [CrossRef] [PubMed]
5. Lee, J.-S.; Tai Kim, S.; Cao, R.; Choi, N.-S.; Liu, M.; Lee, K.T.; Cho, J. Metal-air batteries with high energy density: Li-air *versus* Zn-air. *Adv. Energy Mater.* **2011**, *1*, 34–50. [CrossRef]
6. Cheng, F.; Chen, J. Metal-air batteries: From oxygen reduction electrochemistry to cathode catalysts. *Chem. Soc. Rev.* **2012**, *41*, 2172–2192. [CrossRef] [PubMed]
7. Cao, R.; Lee, J.-S.; Liu, M.; Cho, J. Recent progress in non-precious catalysts for metal-air batteries. *Adv. Energy Mater.* **2012**, *2*, 816–829. [CrossRef]
8. Daniel, C.; Besenhard, J.O. *Handbook of Battery Materials*, 2nd ed.; Wiley-VCH Verlag: Weinheim, Germany, 2011.
9. Li, Y.; Dai, H. Recent advances in zinc-air batteries. *Chem. Soc. Rev.* **2014**, *43*, 5257–5275. [CrossRef] [PubMed]
10. Zhang, J. *PEM fuel cell electrocatalysts and catalyst layers: Fundamentals and applications*; Springer: London, UK, 2008.
11. Katsounaros, I.; Cherevko, S.; Zeradjanin, A.R.; Mayrhofer, K.J.J. Oxygen electrochemistry as a cornerstone for sustainable energy conversion. *Angew. Chem. Int. Ed.* **2014**, *53*, 102–121. [CrossRef] [PubMed]
12. Neburchilov, V.; Wang, H.; Martin, J.J.; Qu, W. A review on air cathodes for zinc-air fuel cells. *J. Power Sources* **2010**, *195*, 1271–1291. [CrossRef]
13. Li, P.-C.; Hu, C.-C.; Lee, T.-C.; Chang, W.-S.; Wang, T.H. Synthesis and characterization of carbon black/manganese oxide air cathodes for zinc-air batteries. *J. Power Sources* **2014**, *269*, 88–97. [CrossRef]
14. Poux, T.; Napolskiy, F.; Dintzer, T.; Kéranguéven, G.; Istomin, S.Y.; Tsirlina, G.; Antipov, E.; Savinova, E. Dual role of carbon in the catalytic layers of perovskite/carbon composites for the electrocatalytic oxygen reduction reaction. *Catal. Today* **2012**, *189*, 83–92. [CrossRef]
15. Lee, J.-S.; Park, G.S.; Lee, H.I.; Kim, S.T.; Cao, R.; Liu, M.; Cho, J. Ketjenblack carbon supported amorphous manganese oxides nanowires as highly efficient electrocatalyst for oxygen reduction reaction in alkaline solutions. *Nano Lett.* **2011**, *11*, 5362–5366. [CrossRef] [PubMed]
16. Malkhandi, S.; Trinha, P.; Manohara, A.K.; Jayachandrababua, K.C.; Kindlerb, A.; Surya Prakasha, G.K.; Narayanana, S.R. Electrocatalytic activity of transition metal oxide-carbon composites for oxygen reduction in alkaline batteries and fuel cells. *J. Electrochem. Soc.* **2013**, *160*, F943–F952. [CrossRef]
17. Cheng, F.; Zhang, T.; Zhang, Y.; Du, J.; Han, X.; Chen, J. Enhancing electrocatalytic oxygen reduction on $MnO_2$ with vacancies. *Angew. Chem. Int. Ed.* **2013**, *52*, 2474–2477. [CrossRef] [PubMed]
18. Xi, L.J.; Wang, H.-E.; Lu, Z.G.; Yang, S.L.; Ma, R.G.; Deng, J.Q.; Chung, C.Y. Facile synthesis of porous $LiMn_2O_4$ spheres as positive electrode for high-power lithium ion batteries. *J. Power Sources* **2012**, *198*, 251–257. [CrossRef]
19. Li, Z.; Ding, Y.; Xiong, Y.; Xie, Y. Rational growth of various $\alpha$-$MnO_2$ hierarchical structures and $\beta$-$MnO_2$ nanorods *via* a homogeneous catalytic route. *Cryst. Growth Des.* **2005**, *5*, 1953–1958. [CrossRef]

20. Gyenge, E.L.; Drillet, J.-F. The electrochemical behavior and catalytic activity for oxygen reduction of $MnO_2$/C– Toray gas diffusion electrodes. *J. Electrochem. Soc.* **2012**, *159*, F23–F34. [CrossRef]
21. Kim, G.; Jeong, S.; Joost, M.; Rocca, E.; Winter, M.; Passerini, S.; Balducci, A. Use of natural binders and ionic liquid electrolytes for greener and safer lithium-ion batteries. *J. Power Sources* **2011**, *196*, 2187–2194. [CrossRef]
22. Escudero, M.J.; Hontañón, E.; Schwartz, S.; Boutonnet, M.; Daza, L. Development and performance characterisation of new electrocatalysts for PEMFC. *J. Power Sources* **2002**, *106*, 206–214. [CrossRef]
23. Gharibi, H.; Kakaei, K.; Zhiani, M. Platinum nanoparticles supported by a vulcan XC-72 and PANI doped with trifluoromethane sulfonic acid substrate as a new electrocatalyst for direct methanol fuel cells. *J. Phys. Chem. C* **2010**, *114*, 5233–5240. [CrossRef]
24. Wiberg, E.; Wiberg, N. *Lehrbuch der anorganischen Chemie*; Walter de Gruyter: Berlin, Germany, 1995.
25. Dhaouadi, H.; Ghodbane, O.; Hosni, F.; Touati, F. $Mn_3O_4$ nanoparticles: Synthesis, characterization and dielectric properties. *ISRN Spectrosc.* **2012**, *2012*, 1–8. [CrossRef]
26. Hamann, C.H.; Vielstich, W. *Elektrochemie, 4., vollst. überarb. und aktualisierte Aufl*; Wiley-VCH: Weinheim, Germany, 2005. (In German)
27. Han, X.; Zhang, T.; Du, J.; Cheng, F.; Chen, J. Porous calcium-manganese oxide microspheres for electrocatalytic oxygen reduction with high activity. *Chem. Sci.* **2012**, *4*, 368–376. [CrossRef]
28. Lima, F.H.; Calegaro, M.L.; Ticianelli, E.A. Investigations of the catalytic properties of manganese oxides for the oxygen reduction reaction in alkaline media. *J. Electroanal. Chem.* **2006**, *590*, 152–160. [CrossRef]
29. Kinoshita, K. *Carbon: Electrochemical and Physicochemical Properties*; Wiley: New York, NY, USA, 1988.
30. Zhou, L.; Zhao, D.; Lou, X.D. $LiNi_{0.5}Mn_{1.5}O_4$ hollow structures as high-performance cathodes for lithium-ion batteries. *Angew. Chem.* **2012**, *124*, 243–245. [CrossRef]
31. Masa, J.; Xia, W.; Sinev, I.; Zhao, A.; Sun, Z.; Grützke, S.; Weide, P.; Muhler, M.; Schuhmann, W. Eine stickstoff-dotierte kohlenstoffmatrix mit eingeschlossenen $Mn_xO_y$/NC- und CoxOy/NC-nanopartikeln für leistungsfähige bifunktionale Sauerstoffelektroden. *Angew. Chem.* **2014**, *126*, 8648–8652. [CrossRef]